JGR Space Physics

RESEARCH ARTICLE
10.1029/2022JA030542

Key Points:

- Electric field variations by medium-scale traveling ionospheric disturbances (MSTIDs) are not always observed in the magnetosphere
- Magnetosphere-ionosphere coupling of MSTIDs depends on the Kp index and the amplitude of the MSTIDs
- Arase observed electric field and electron density variations associated with MSTIDs by both plasma instabilities and gravity waves

Supporting Information:

Supporting Information may be found in the online version of this article.

Correspondence to:

K. Shiokawa,
shiokawa@nagoya-u.jp

Citation:

Kawai, K., Shiokawa, K., Otsuka, Y., Oyama, S., Connors, M. G., Kasahara, Y., et al. (2023). Multi-event analysis of magnetosphere-ionosphere coupling of nighttime medium-scale traveling ionospheric disturbances from the ground and the Arase satellite. *Journal of Geophysical Research: Space Physics*, *128*, e2022JA030542. https://doi.org/10.1029/2022JA030542

Received 10 APR 2022
Accepted 4 JAN 2023

Author Contributions:

Conceptualization: K. Kawai, K. Shiokawa
Data curation: K. Kawai, K. Shiokawa, Y. Otsuka, S. Oyama, M. G. Connors, Y. Kasahara, Y. Kasaba, S. Nakamura, F. Tsuchiya, A. Kumamoto, A. Shinbori, A. Matsuoka, I. Shinohara, Y. Miyoshi
Formal analysis: K. Kawai, S. Nakamura
Funding acquisition: K. Shiokawa, M. G. Connors, Y. Kasahara, Y. Kasaba, I. Shinohara, Y. Miyoshi
Investigation: K. Kawai, K. Shiokawa
Methodology: K. Kawai, K. Shiokawa, A. Shinbori
Project Administration: K. Shiokawa, M. G. Connors, Y. Kasahara, Y. Kasaba, A. Matsuoka, I. Shinohara, Y. Miyoshi

Multi-Event Analysis of Magnetosphere-Ionosphere Coupling of Nighttime Medium-Scale Traveling Ionospheric Disturbances From the Ground and the Arase Satellite

K. Kawai[1], K. Shiokawa[1], Y. Otsuka[1], S. Oyama[1,2,3], M. G. Connors[4], Y. Kasahara[5], Y. Kasaba[6], S. Nakamura[1], F. Tsuchiya[6], A. Kumamoto[6], A. Shinbori[1], A. Matsuoka[7], I. Shinohara[8], and Y. Miyoshi[1]

[1]Institute for Space-Earth Environmental Research, Nagoya University, Nagoya, Japan, [2]National Institute of Polar Research, Tachikawa, Japan, [3]University of Oulu, Oulu, Finland, [4]Athabasca University, Athabasca, Alberta, Canada, [5]Graduate School of Natural Science and Technology, Kanazawa University, Kanazawa, Japan, [6]Tohoku University, Sendai, Japan, [7]Kyoto University, Kyoto, Japan, [8]Institute of Space and Astronautical Science, Japan Aerospace Exploration Agency, Sagamihara, Japan

Abstract Kawai et al. (2021) reported the first ground-satellite conjugate observation of nighttime medium-scale traveling ionospheric disturbances (MSTIDs), by analyzing measurements from an airglow imager at Gakona (geographic latitude: 62.39°N, geographic longitude: 214.78°E, magnetic latitude: 63.60°N) and the Arase satellite in the magnetosphere on 3 November 2018. The Arase satellite observed variations in both the polarization electric field and the electron density as the Arase footprint passed through the MSTID structures in the ionosphere. In this study, we investigated whether these electric field and density variations associated with MSTIDs at subauroral latitudes are always observed by Arase in the magnetosphere. We used three airglow imagers installed at Gakona, Athabasca (geographic latitude: 54.60°N, geographic longitude: 246.36°E, magnetic latitude: 61.10°N), and Kapuskasing (geographic latitude: 49.39°N, geographic longitude: 277.81°E, magnetic latitude: 58.70°N) and the Arase satellite. We found eight observations of MSTIDs conjugate with Arase. They indicate that electric field and density variations associated with MSTIDs are not always observed in the magnetosphere. These variations tend to be observed in the magnetosphere during geomagnetically quiet times and when the amplitude of the MSTID is large. We categorized the MSTIDs into those caused by plasma instabilities and gravity waves and found that the electric field and density variations can be observed in the magnetosphere for both types of MSTIDs.

Plain Language Summary Medium-scale traveling ionospheric disturbances (MSTIDs) involve the propagation of electron density perturbations in the ionosphere. Kawai et al. reported an event in which MSTIDs were generated in the magnetosphere-ionosphere coupled system using an airglow imager at Gakona (62.39°N, 214.78°E, 63.60°MLAT) and the Arase satellite. This was the first conjugate observation of nighttime MSTIDs with a magnetospheric satellite. In this study, we investigate whether those electric field and density variations associated with MSTIDs are always observed by Arase in the inner magnetosphere. We found eight conjugate observations of nighttime MSTIDs using airglow imagers at Gakona, Athabasca (54.60°N, 246.36°E, 61.10°MLAT), and Kapuskasing (49.39°N, 277.81°E, 58.70°MLAT) and the Arase satellite. They indicate that electric field and density variations associated with MSTIDs are not always observed in the magnetosphere. These variations tend to be observed in the magnetosphere during geomagnetically quiet times and when the amplitude of the MSTID is large. We categorized the MSTIDs into those caused by plasma instabilities and gravity waves and found that the electric field and density variations can be observed in the magnetosphere for both types of MSTIDs.

1. Introduction

Traveling ionospheric disturbances (TIDs) are phenomena in which electron density perturbations in the ionosphere propagate with wave-like structures. Hunsucker (1982) defined medium-scale TIDs (MSTIDs) when horizontal velocity, oscillation period, and horizontal wavelength are in the range of 100–250 m/s, 15–60 min, and several hundred kilometers, respectively. MSTIDs are frequently observed at middle latitudes, but also at low and high latitudes. MSTIDs have been widely studied for a long time by using various instruments such as airglow

Resources: K. Kawai, K. Shiokawa, S. Oyama, M. G. Connors, Y. Kasahara, Y. Kasaba, S. Nakamura, F. Tsuchiya, A. Kumamoto, A. Matsuoka, I. Shinohara, Y. Miyoshi
Software: K. Kawai, Y. Otsuka, S. Nakamura, A. Shinbori
Supervision: K. Shiokawa
Validation: K. Kawai, K. Shiokawa, Y. Otsuka, Y. Kasaba, S. Nakamura, F. Tsuchiya, A. Kumamoto, A. Shinbori, A. Matsuoka, Y. Miyoshi
Visualization: K. Kawai
Writing – original draft: K. Kawai
Writing – review & editing: K. Kawai, K. Shiokawa, Y. Otsuka, S. Oyama, M. G. Connors, Y. Kasaba, S. Nakamura, Y. Miyoshi

imagers (e.g., Mendillo et al., 1997; Taylor et al., 1998), ionosondes (Bowman, 1990), and total electron content (TEC) detectors (e.g., Otsuka et al., 2013; Saito et al., 1998).

Several studies have been conducted to understand the characteristics and generation mechanism of nighttime MSTIDs. Nighttime MSTIDs in the middle latitudes are believed to be caused by the Perkins instability (Perkin, 1973). However, the growth rate of the MSTIDs is too small to support measurements. Vertical coupling processes between ionospheric E and F region significantly affect the growth of the MSTIDs (Cosgrove & Tsunoda, 2001, 2004; Yokoyama et al., 2004, 2009; Yokoyama & Hysell, 2010; Narayanan et al., 2018). High-latitude MSTIDs show sudden change of their propagation directions associated with auroral brightening and geomagnetic disturbances (Shiokawa et al., 2012; Yadav et al., 2020). Gravity waves in the neutral atmosphere are another cause of MSTIDs (e.g., Fukushima et al., 2012; Moral et al., 2019). Kubota et al. (2011) and Shiokawa et al. (2013) reported that some MSTIDs observed in airglow images at subauroral latitudes show characteristics of gravity waves in the thermosphere. Polarization electric field can be created by gravity waves in the thermosphere due to neutral wind oscillations and the F-region dynamo (e.g., Chou et al., 2018; Liu & Vadas, 2013). The polarization electric fields associated with the growth and generation of the MSTIDs are mapped to the topside of the ionosphere along the magnetic field lines (Shiokawa et al., 2003). Then the first conjugate observations of MSTIDs were reported by Otsuka et al. (2004) and Shiokawa et al. (2005) using airglow imagers in Japan and Australia. They showed that MSTIDs have mirrored structures at the geomagnetically conjugate points at both hemispheres in the Asian sector. The conjugacy of MSTIDs in the American and Europe-Africa longitudinal sectors was shown by Martinis et al. (2011, 2018). Chou et al. (2022) reported geomagnetic conjugacy of MSTIDs caused by electrodynamic coupling of tsunami/volcano-induced gravity waves with ionospheric plasma.

Recently Kawai et al. (2021) reported that the Arase satellite in the inner magnetosphere observed the electric field variations associated with the MSTID that was captured in the 630.0-nm airglow images at Gakona, Alaska, on 3 November 2018 at subauroral latitudes. Arase also observed the electron density fluctuations which are caused by $\mathbf{E} \times \mathbf{B}$ drift of magnetospheric plasma by the electric field variations associated with MSTIDs. However, their report of magnetosphere-ionosphere coupling of MSTIDs was limited for only one event, because of difficulty to find out good conjugate measurement of MSTIDs by airglow imagers and magnetospheric satellites.

In this paper, based on multi-point ground-satellite observations of MSTIDs over 4 years, we present multi-event study of nighttime MSTIDs using all-sky airglow imagers in North America (Athabasca, Gakona, and Kapuskasing) at subauroral latitudes and the Arase satellite flying near the equatorial plane of the inner magnetosphere, in order to check whether the electric field and electron density variations associated with MSTIDs are always mapped to the magnetosphere. We found that the MSTIDs did not always show the magnetosphere-ionosphere correspondence. Clear magnetosphere-ionosphere correspondence of MSTIDs tends to be observed under geomagnetically quiet condition and with larger amplitude of the MSTIDs. We categorized the MSTIDs into those caused by plasma instabilities and gravity waves and found that both types of MSTIDs show mapping to the magnetosphere.

2. Instrumentation

2.1. Exploration of Energization and Radiation in Geospace (ERG)

The exploration of energization and Radiation in Geospace (ERG) satellite, also named as Arase, was launched on 20 December 2016 to investigate how energetic particles are generated and lost, and how space storms are developed (Miyoshi, Shinohara, et al., 2018). The Arase satellite is in an elliptical Earth orbit (perigee: ~440 km, apogee: ~32,000 km) with a period of ~570 min and is equipped with several instruments. In this study, we use the High-Frequency Analyzer (HFA) (Kasahara, Kumamoto, et al., 2018; Kumamoto et al., 2018) and the Electric Field Detector (EFD) (Kasaba et al., 2017; Kasahara, Kasaba, Matsuda, et al., 2018) of the Plasma Wave Experiment (PWE) (Kasahara, Kasaba, Kojima, et al., 2018), and the Magnetic Field Experiment (MGF) (Matsuoka, Teramoto et al., 2018; Matsuoka et al., 2018a, 2018b). The Arase data in this study are analyzed by the Space Physics Environment Data Analysis Software (SPEDAS) tool (Angelopoulos et al., 2019).

2.2. Ground-Based Airglow Imagers at Subauroral Latitudes and Conjugate Event Search

We use several criteria to sort out the conjugate observations of MSTIDs using airglow imagers and the Arase satellite. We first use 10 airglow imagers of the Optical Mesosphere Thermosphere Imagers (OMTIs, Shiokawa et al., 1999, 2017) at Athabasca and Kapuskasing in Canada, Paratunka, Magadan, Zhigansk, and Istok in Russia, Tromsø in Norway, Nyrölä in Finland, Gakona in Alaska, and Húsafell in Ísland, over 4 years of April 2017–April

Table 1
List of the Specifications of Imager #7, #16, and #19

Filter number	Species	Observation wavelength [nm]	Filter bandwidth [nm]	Typical sensitivity [count/r/s]	Exposure time [s]	Binning
Camera #7 (C7, Athabasca, 512 × 512 pixels)						
1	OI	557.7	1.760	0.2000	5	2 × 2
2	OI	630.0	1.650	0.3190	30	2 × 2
3	OH	720–910	190.000	–	1	2 × 2
4	H-beta	486.1	1.320	0.1930	40	2 × 2
5	background	572.5	1.630	0.2140	15	2 × 2
6	OI	844.6	1.200	0.1480	25	2 × 2
7	Na	589.3	1.500	0.5430	15	2 × 2
Camera #16 (CG, Kapuskasing, 1,024 × 1,024 pixels)						
1	OI	557.7	1.783	0.5185	15	2 × 2
2	OI	630.0	1.644	0.5343	30	2 × 2
3	OH	>720	–	–	1	2 × 2
4	H-beta	486.1	1.346	0.3558	30	2 × 2
5	background	572.5	1.498	0.4542	30	2 × 2
Camera #19 (CJ, Gakona, 1,024 × 1,024 pixels)						
1	OI	557.7	1.781	0.4966	15	2 × 2
2	OI	630.0	1.685	0.5504	30	2 × 2
3	OH	>720	–	–	1	2 × 2
4	H-beta	486.1	1.364	0.3621	30	2 × 2
5	Background	572.5	1.492	0.4586	30	2 × 2

2021. Details of airglow imagers of OMTIs at these stations are shown by Shiokawa et al. (1999, 2017, also at https://stdb2.isee.nagoya-u.ac.jp/omti/index.html). The airglow images obtained at these stations were categorized into four levels of sky condition every hour by visual inspection, that is, (a) clear sky with stars, (b) a few clouds and many stars, (c) many clouds and a few stars, and (d) overcast or rain. The 3,100 nights which include sky condition (a) or (b) were the target of simultaneous observations. Then, we chose the 443 nights when the Arase footprint passed through the field-of-view (FOV) of imagers at the time of sky condition (a) or (b). We defined the imager FOV as ±10.24° in latitude and longitude from the station location. The Arase footprints used in this procedure are those stored in the Arase database and are those projected onto the ionosphere of the northern hemisphere at an altitude of 100 km using the Tsyganenko-Sytnov 05 (TS05) model (Tsyganenko & Sitnov, 2005). This Arase footprint database enables us to save time for calculation of the footprint location. Next, by visual inspection we selected the 85 nights for which the MSTIDs were observed in the 630-nm airglow deviation images. The airglow deviation images were obtained by subtracting 1-hr running averages from raw images to clearly show the structures temporally and spatially variated. Finally, we selected eight events for which Arase footprints crossed the MSTID phase fronts. These eight events were obtained at three stations shown in Table 1, that is, Athabasca, Canada (geographic latitude (GLAT): 54.60°N, geographic longitude (GLON): 246.36°E; magnetic latitude (MLAT): 61.1°N), Kapuskasing, Canada (GLAT: 49.39°N, GLON: 277.81°E; MLAT: 58.7°N), and Gakona, Alaska (GLAT: 62.39°N, GLON: 214.78°E; MLAT: 63.6°N). In this procedure, the footprints were mapped onto the ionosphere at an altitude of 250 km using the Tsyganenko 01 (T01) model (Tsyganenko, 2002a, 2002b), because the MSTIDs in the present analysis were observed during geomagnetically quiet time when the T01 model is more suitable for field-line mapping (Chen et al., 2006).

The specifications of the all-sky imagers (imager #7 (Athabasca), #16 (Kapuskasing), and #19 (Gakona)) used in this study are shown in Table 1, based on Shiokawa et al. (2017). All these imagers have five filters at wavelengths of 557.7 nm (oxygen atoms), 630.0 nm (oxygen atoms), 720–1,000 nm (OH-band), 486.1 nm (hydrogen atoms), and 572.5 nm (background) for channels 1–5. The bandwidths of these filters are 1.320–1.783 nm except for OH-band filters. In this analysis, 630.0-nm and 572.5-nm images were used to identify the MSTIDs. The 557.7-

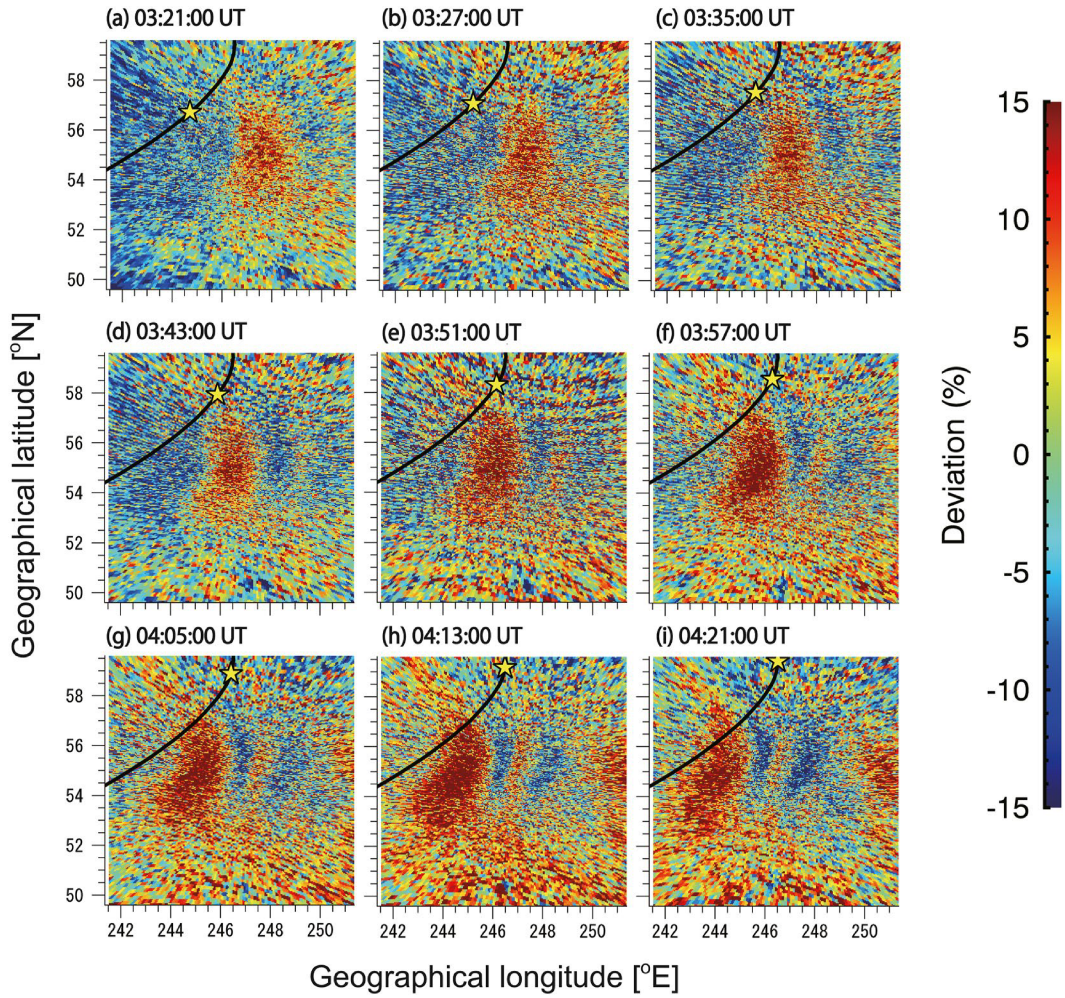

Figure 1. The 630.0-nm airglow deviation images at Athabasca on 25 February 2020. The images are in geographical coordinates of 10° × 10° by assuming that a 630.0-nm airglow emission layer is at an altitude of 250 km. Black curves and yellow stars indicate the Arase satellite trajectory and the footprint projected onto the ionosphere using the Tsyganenko 01 (T01) model (Tsyganenko, 2002a, 2002b), respectively.

nm and OH images were also used to distinguish MSTID structures from clouds and auroras, because clouds and auroras show similar structures in 557.7-nm, 630-nm, and OH images, while MSTIDs can be seen only in 630-nm images. The 572.5-nm images are used to subtract continuous background emission to acquire the absolute intensity of 630.0-nm images. The imagers' charge-coupled devices (CCDs) have 1,024 × 1,024 pixels at Gakona and Kapuskasing and 512 × 512 at Athabasca. 2 × 2 binning was applied on the device to increase output count, resulting in an image size of 512 × 512 and 256 × 256 pixels, respectively.

3. Observations

Case 1. Good correspondence event on 25 February 2020 at Athabasca

Figure 1 shows 630.0-nm airglow deviation images taken at 0321:00–0421:00 UT (1921:00–2021:00 LT) on 25 February 2020 at Athabasca, Canada. We use the 630.0-nm airglow deviation images obtained by subtracting 1-hr running averages of airglow intensity from raw images to discuss the perturbations in the airglow intensity. These airglow deviation images are converted to geographical coordinates by assuming that a 630.0-nm airglow emission layer exists at an altitude of 250 km. The black curves and the yellow stars indicate the Arase satellite trajectory and footprint mapped at an altitude of 250 km using the Tsyganenko 01 (T01) model (Tsyganenko, 2002a, 2002b). The horizontal and vertical axes show the geographical longitude and latitude, respectively.

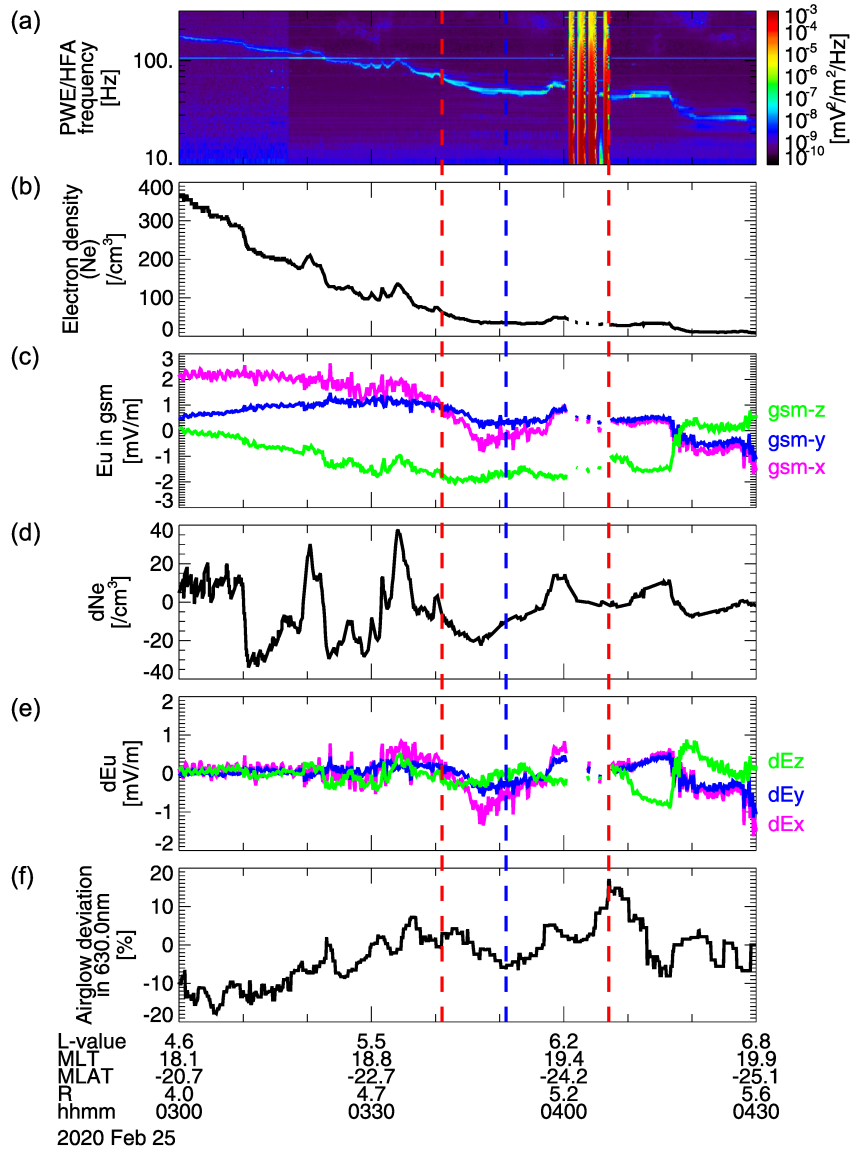

Figure 2. Arase satellite data observed at 0300–0430 UT on 25 February 2020, for (a) UHR frequency of electric field spectra (level 2/version 1.02), (b) electron density, (c) electric field in GSM coordinates measured by u-sensor of the EFD (level 2/version 5.01), (d) electron density fluctuations, (e) electric field variations in GSM coordinates calculated by subtracting 30-min running averages, (f) 630.0-nm airglow deviations at the footprint of the Arase satellite. The labels below the horizontal axis indicate the McIlwain L value derived from the IGRF-13 model (Alken et al., 2021), magnetic local time (MLT), magnetic latitude (MLAT), and radial distance from Earth (Re), and time (UT). The vertical red and blue dashed lines show when the Arase satellite footprint crossed the bright and dark parts of the MSTIDs, respectively.

During this event, MSTIDs with a wavefront elongated north-south (N-S) were observed at the center part of the images in Figure 1. The MSTIDs appeared at 247°–250°E and 53°–57°N starting at ~0300 UT (before the time shown in Figure 1), and propagated westward. The footprint of the Arase satellite crossed the northern parts of the wavefront at 246°–247°E and 57°–59°N from 0335:00 to 0405:00 UT. We estimated a wavelength of ~161 km, a period of ~40 min, and a zonal phase velocity of ~68 m/s for these MSTIDs from the E-W keogram (shown in Figure S8 in Supporting Information S1). These values roughly match the characteristic MSTID parameters shown by Hunsucker (1982).

Figure 2 shows (a) upper hybrid resonance (UHR) frequency of electric field spectra obtained by PWE/HFA, (b) electron density calculated from the UHR waves appearing in the spectra of Figure 2a and the ambient magnetic field measured by MGF, (c) electric field in geocentric solar magnetospheric (GSM) coordinates measured by

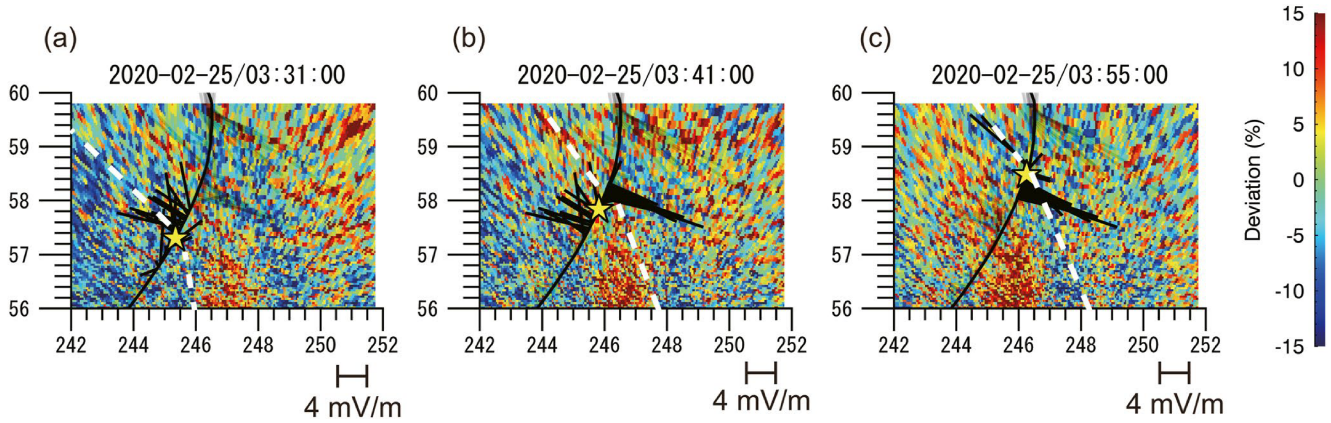

Figure 3. The electric field variations observed by Arase and the MSTIDs in the 630.0-nm airglow images at Athabasca. The black curves extending south to north are the trajectory of Arase projected onto the ionosphere. The electric field variations are those shown in Figure 2e, mapped from the magnetosphere to the ionosphere, and shown on the satellite trajectory by black lines. Each image shows only the electric field variations for 10 min before and after each time. The yellow star is the Arase satellite footprint at corresponding time. The white dashed lines determined by visual inspection indicate the bright-dark boundaries of the MSTID near the satellite footprint. The horizontal and vertical axis show the geographical longitude and latitude, respectively.

u-sensor of the EFD, (d) electron density fluctuations, (e) electric field variations in the GSM coordinates, (f) 630.0-nm airglow deviations at the footprint of Arase. We subtracted apparent electric fields due to satellite motion in background geomagnetic field and due to corotation of the plasma with the Earth's rotation, in order to obtain the electric field in Figure 2c. The variations in Figure 2d (electron density) and Figure 2e (electric field) were calculated by subtracting 30-min running averages from those plotted in Figures 2b and 2c, respectively. Because the time interval that the Arase satellite passes through the peak-to-peak of the MSTIDs is 20–30 min, we apply the 30-min running average so that Figures 2d and 2e focus only on the waves with periods of less than 30 min. The horizontal axis is 0300–0430 UT. The angle between the satellite's spin plane and the local magnetic field varied from ∼12° at 0300 UT to ∼30° at 0430 UT. The vertical red and blue dashed lines show the period during which the footprint of Arase passed through the bright and dark parts of the MSTID, respectively. These timings were determined based on the airglow images with satellite footprints shown in Figure 1. Because of the noise of the images and because the footprint passed through just north of the MSTID structure, the red lines are not always at the location of maximum intensity in Figure 2f. The strong vertically extended signals at 0400–0406 UT in Figure 2a are artificial calibration signal. We could determine UHR frequencies only intermittently during this period.

The waveform showing the electron density fluctuations (Figure 2d) and the airglow deviations at the footprint of Arase (Figure 2f) are very similar in the interval around the MSTID crossing. The correlation coefficient between electron density fluctuations and the airglow deviations at the footprint of Arase is 0.426 during 0341–0407 UT (shown by red dashed lines) when the Arase satellite passed the phase fronts of the MSTIDs. The x- and y-components of the electric field variations in GSM coordinates and the airglow deviations at the footprint of Arase are also positively correlated.

We projected the electric field variations observed by Arase onto the ionosphere at an altitude of 250 km to compare them with the MSTIDs observed by the airglow imager. Figure 3 shows the comparison of the MSTIDs observed by the airglow imager and the electric field variations observed by Arase. The black curves extending from the south (244°E, 56°N) to the north (246°E, 60°N) are the trajectory of Arase projected onto the ionosphere. The electric field variations in the ionosphere are calculated from the electric field observed by Arase, assuming equipotential magnetic field lines (T01 model). They are indicated by black lines on Arase's trajectory in Figure 3. Each image of Figure 3 shows only the electric field variations for 10 min before and after each time. The yellow star is the Arase satellite footprint at corresponding time. The white dashed lines in each image indicate the bright-dark boundaries of the MSTIDs near the satellite footprint. The horizontal and vertical axis show the geographical longitude and latitude, respectively.

The direction of the mapped electric field variations tends to point west-northwestward in the larger airglow intensity region, while they point east-southeastward in the lower airglow intensity region. Throughout all images in Figure 3, the direction of electric field variations reverses at the bright and dark boundaries of the MSTID. The

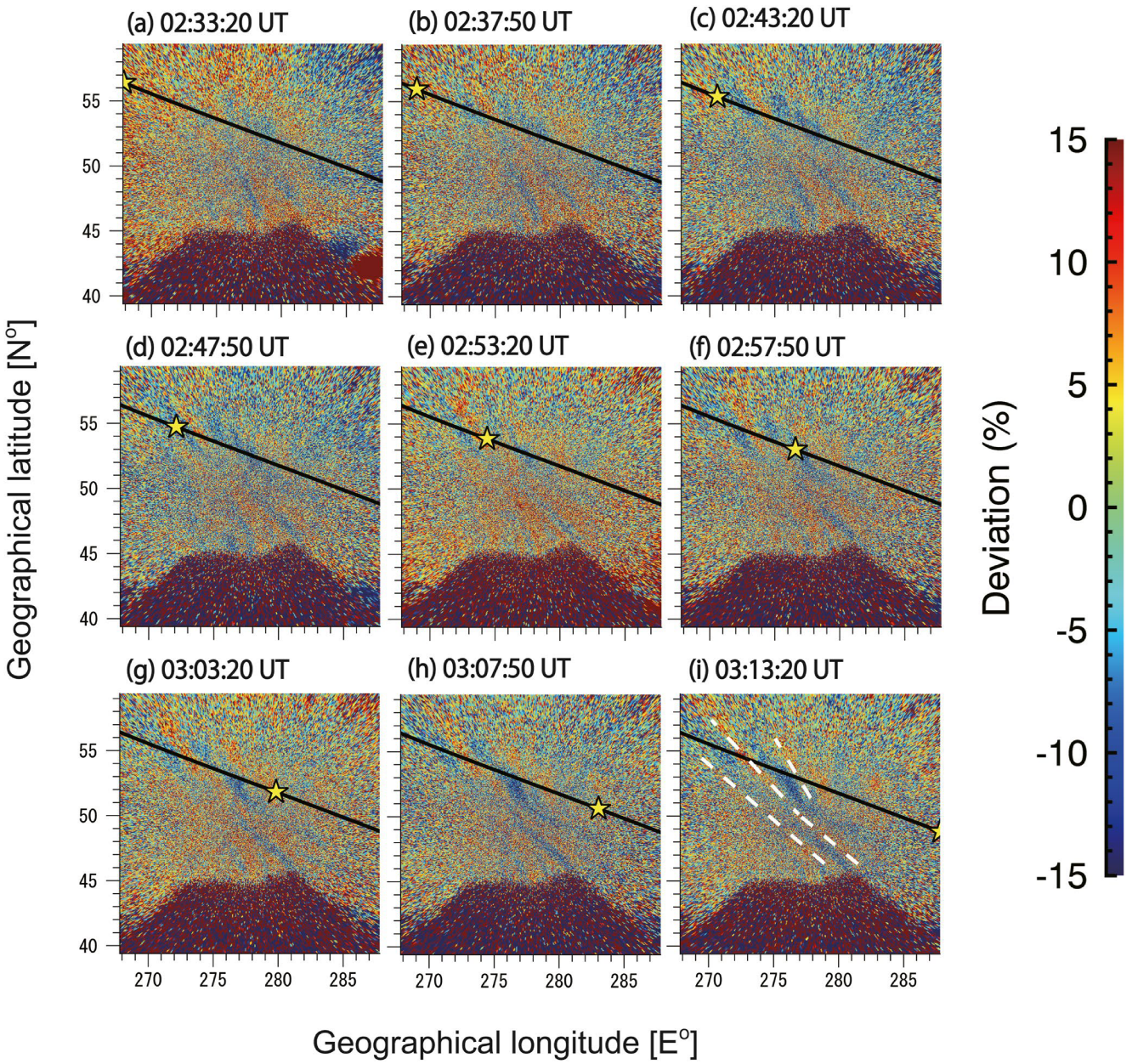

Figure 4. The 630.0-nm airglow deviation images at Kapuskasing on 26 January 2019. The images are in geographical coordinates of 20° × 20° at an altitude of 250 km using the T01 model. Black curves and yellow stars indicate the Arase satellite trajectory and the footprint projected onto the ionosphere, respectively. The dark area at bottom part of each image is a mask to avoid a city-light.

amplitude of mapped electric field variations is ~10 mV/m. These good correspondences between electric field and airglow deviations are very similar to the observation reported by Kawai et al. (2021).

Case 2. No correspondence event on 26 November 2019 at Kapuskasing

Figure 4 shows 630.0-nm airglow deviation images taken at 0233:20–0313:20 UT (2133:20-2213:20 LT) on 26 January 2019 at Kapuskasing, Canada. These airglow deviation images are converted to geographical coordinates by assuming that the 630.0-nm airglow emission layer exists at an altitude of 250 km. The black curves and the yellow stars indicate the Arase satellite trajectory and footprint mapped at an altitude of 250 km using the T01 model.

In this event, the MSTIDs had a wavefront elongated from northwest-southeast (NW-SE) and propagated westward. The MSTIDs appeared at 270°–285°E and 45°–55°N in these images (white dashed lines in Figure 4i). The

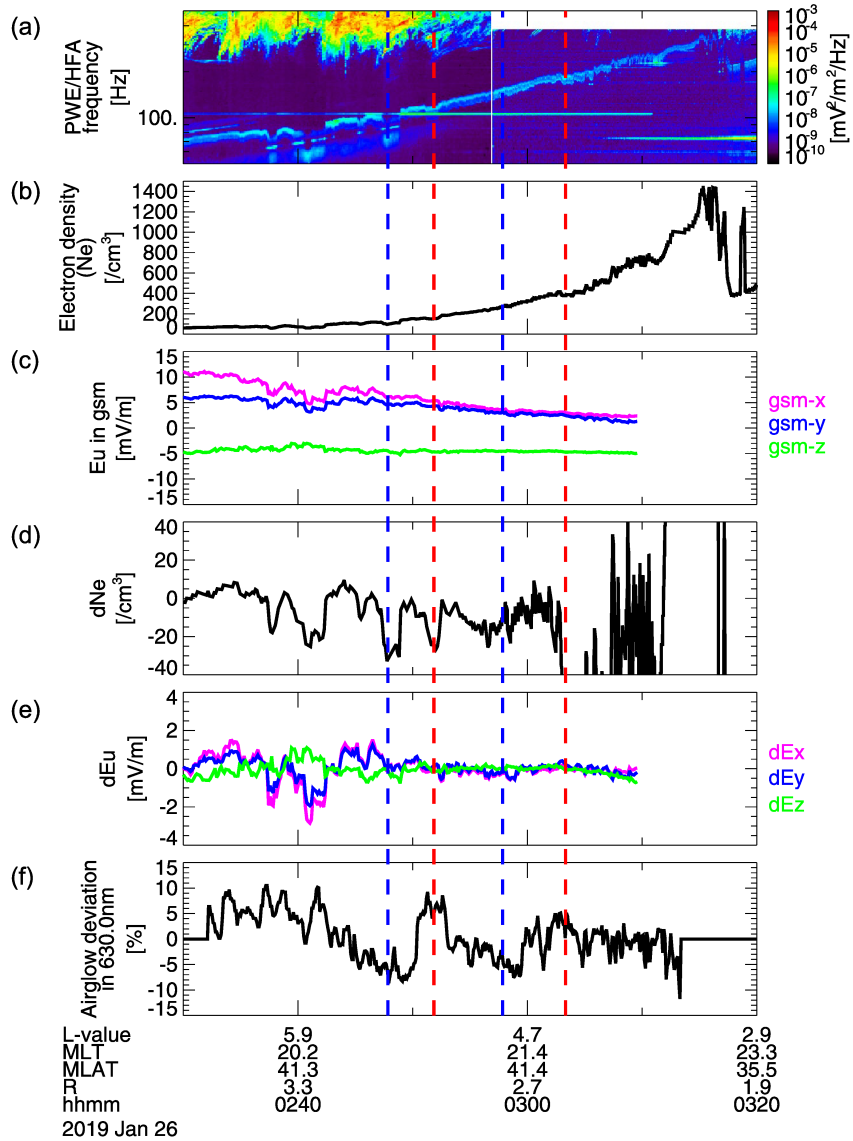

Figure 5. Arase satellite data observed at 0230–0320 UT on 26 January 2019 for (a) UHR frequency of electric field spectra, (b) electron density, (c) electric field in GSM coordinates measured by u-sensor of the EFD, (d) electron density fluctuations, (e) electric field variations in GSM coordinates calculated by subtracting 15-min running averages, (f) 630.0-nm airglow deviations at the footprint of the Arase satellite. The labels below the horizontal axis indicate the McIlwain L value, MLT, MLAT, Re, and UT. The vertical red and blue dashed lines show when the Arase satellite footprint crossed the bright and dark parts of the MSTIDs, respectively.

footprint of the Arase satellite crossed the wavefront at 272°–281°E and 52°–55°N from 0243:20 UT to 0303:20 UT. We estimated a wavelength of ~239 km, a period of ~47 min, and a zonal phase velocity of ~76 m/s for these MSTIDs from the E-W keogram (shown in Figure S14 in Supporting Information S1). These values roughly match the characteristic MSTID parameters shown by Hunsucker (1982).

Figure 5 shows (a) UHR frequency of electric field spectra, (b) electron density, (c) electric field in the GSM coordinates, (d) electron density fluctuations, (e) electric field variations in the GSM coordinates, (f) 630.0-nm airglow deviations at the footprint of Arase. The apparent electric fields due to satellite motion and the rotation of the Earth were subtracted in the electric field in Figure 5c. The variations in Figure 5d (electron density) and Figure 5e (electric field) were calculated by subtracting 15-min running averages from the data plotted in Figures 5b and 5c, respectively. Because the time interval that the Arase satellite passes through the peak-to-peak of the MSTIDs is ~10 min, we apply the 15-min running average so that Figures 5d and 5e focus only on the

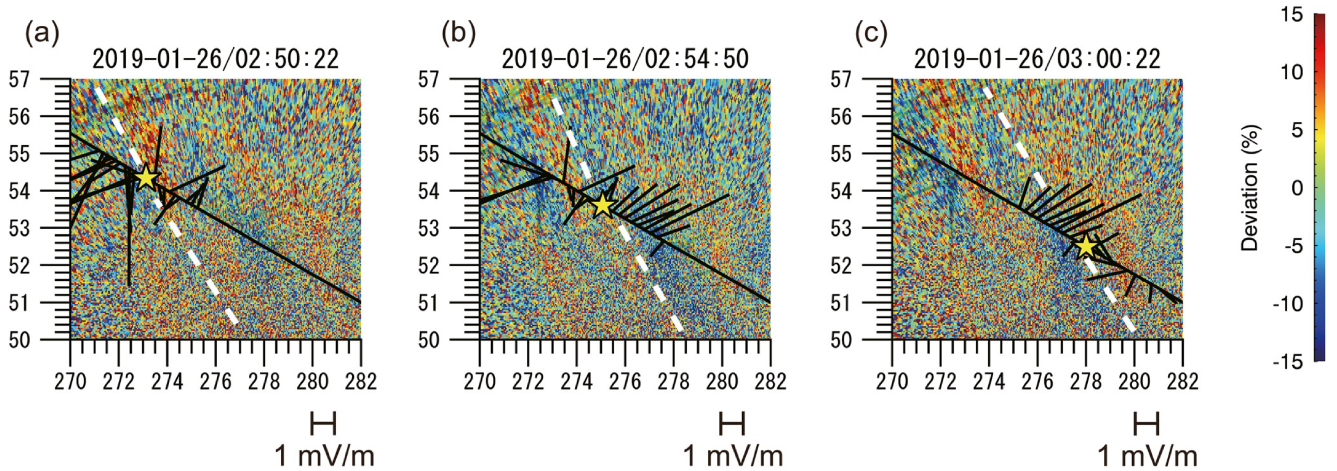

Figure 6. The electric field variations observed by Arase and the MSTID in the 630.0-nm airglow images at Kapuskasing. The black curves extending south to north are the trajectory of Arase projected onto the ionosphere. The electric field variations in the ionosphere are those shown in Figure 5e, mapped from the magnetosphere to the ionosphere, and shown on this trajectory by black lines. Each image shows only the electric field variations for 5 min before and after each time. The yellow star is the Arase satellite footprint at that time. The white dashed lines indicate the bright-dark boundaries of the MSTID near the satellite footprint. The horizontal and vertical axis show the geographical longitude and latitude, respectively.

waves with periods of less than 15 min. The horizontal axis is 0230–0320 UT. The angle between the satellite's spin plane and the local magnetic field varied from ∼15° at 0230 UT to ∼48° at 0320 UT. Again, the vertical red and blue dashed lines show the period during which the footprint of Arase passed through the bright and dark parts of the MSTID, respectively, based on Figure 4.

From Figures 5d–5f, the electric field variations and electron density variations observed by Arase seem not to synchronize with the airglow deviations at the footprint of Arase. The electric field variation in Figure 5f does not show any significant variation in the time scale of airglow variation. The correlation coefficient between electron density fluctuations and the airglow deviations at the footprint of Arase is 0.092 during 0247:50–0303:20 UT (interval from leftmost blue to rightmost red dashed lines) when the Arase satellite passed the phase fronts of the MSTIDs.

Figure 6 shows the comparison of the MSTIDs observed by the airglow imager and the electric field variations observed by Arase. The black curves extending from the west (270°E, 55.5°N) to the east (282°E, 51°N) are the trajectory of Arase projected onto the ionosphere. The electric field variations in the ionosphere are indicated by black lines on Arase's trajectory in Figure 6. Each image of Figure 6 shows only the electric field variations for 5 min before and after each time. The yellow star is the Arase satellite footprint at that time. The white dashed lines of each images indicate the bright-dark boundaries of the MSTIDs near the satellite footprint. The horizontal and vertical axis show the geographical longitude and latitude, respectively.

The maximum amplitude of mapped electric field variations is ∼3 mV/m. The direction of the electric field variations seems to change before and after the footprint of Arase. However, the direction of the electric field variations during 0250:20–0254:50 UT (time from Figure 6a to Figure 6b) was not unidirectional, even though the footprint of Arase was located in the bright part of the MSTIDs. Before 0250:22 UT, the footprint was located in the dark part of the MSTIDs, and the direction of the electric field variations is southwestward. On the other hand, during 0254:50–0300:22 UT (time interval from Figure 6b to Figure 6c), the footprint was also located in the dark part of the MSTIDs, but the direction of the electric field variations is northeastward.

4. Multi-Event Analysis and Discussion

As shown in the two examples in Section 3, we found eight conjugate observations of nighttime MSTIDs using airglow imagers at Athabasca, Gakona, and Kapuskasing and the Arase satellite. The all-sky images with Arase footprints, similar to Figures 1 and 4, are shown in Figures S1–S6 in Supporting Information S1 for the other six events. The longitudinal cross sections (keograms) of all-sky images to show motion of these MSTIDs for all the eight events are shown in Figures S7–S14 in Supporting Information S1. We base the overall discussion on these eight events.

Figures 7 and 8 show (top) the electron density fluctuations, (middle) electric field variations in the field-aligned (FA) coordinates, and (bottom) airglow deviations at the footprint of Arase for all eight events. The FA coordinate system consists of azimuth, radial, and parallel to the background magnetic field lines. In Figures 7 and 8, the azimuth and radial components of the electric field variations are plotted in the middle panel. The parallel component of the electric field was assumed to be zero when we calculated the azimuth and radial components of the electric field from the two-wire antenna data of Arase. Apparent electric fields due to satellite motion and Earth's rotation were subtracted. The airglow deviations in these figures are obtained by subtracting 1-hr running averages. The variations of electron density and electric fields were calculated by subtracting running averages with time scales of 15 min (Figures 7g–7i, 8d, 8e, 8f, 8g, 8h, 8i, 8j, 8k and 8l), 20 min (Figures 7a–7c, 7j, 7k, 7l, 8a, 8b and 8c), and 30 min (Figures 7d–7f). These time scales of running average subtraction were determined to match with the time scales of satellite crossing of the MSTID structures, as shown in cases 1 and 2 in Section 3. Note that the velocity of the ionospheric footprint of Arase significantly varies depending on the radial distance of the satellite from the Earth.

Figure 7 shows events (a, b, c) at Athabasca on 1 January 2019, (d, e, f) at Athabasca on 25 February 2020, (g, h, i) at Athabasca on 26 November 2020, (j, k, l) at Gakona on 3 November 2018. Figure 8 shows events all at Kapuskasing (a, b, c) on 7 July 2018, (d, e, f) on 10 August 2018, (g, h, i) on 11 January 2019, (j, k, l) on 26 January 2019. The events shown in Figures 7d–7f and 8j–8l are cases 1 and 2 in Section 3, respectively. The vertical red and blue dashed lines in Figures 7 and 8 show when the Arase satellite footprint crossed the bright and dark parts of the MSTIDs, respectively.

In Figures 7a–7c, both density and electric field variations do not show clear correspondence with the airglow variations in the bottom panel, though the airglow variations associated with MSTIDs are rather clear. In Figures 7d–7f, density, radial component of electric field, and airglow deviations have similar waveforms during 0341:00–0407:00 UT (interval from leftmost red to rightmost red dashed lines). In Figures 7g–7i, Arase did not observe electric field variations associated with airglow deviations of the MSTIDs in Figure 7i. The density variation in Figure 7g is small, but some correspondence is seen associated with the MSTIDs, as shown later. In Figures 7j–7l, density variations and airglow deviations are negatively correlated. Radial component of electric field variations is positively correlated with airglow deviations, while azimuth component of electric field variations is negatively correlated with airglow deviations.

In Figures 8a–8c, no Arase electric field data are available during this event. Density variations are negatively correlated with airglow deviations of the MSTIDs. In Figures 8d–8f, density variations are positively correlated with the airglow deviations (similar decreasing trends in both data between the two dashed lines). Azimuth and radial components of electric field variations show positive and negative correspondence with airglow deviations, respectively. In Figures 8g–8i, the waveforms of density variations and airglow deviations are similar. However, they did not show clear correspondence. In Figures 8j–8l, both density and electric field variations did not show correspondence with the airglow deviations.

Nighttime MSTIDs are expected to accompany polarization electric field due to variation of conductivity and background ionospheric current (e.g., Perkin, 1973; Shiokawa et al., 2003; Yokoyama et al., 2009). The 630-nm airglow intensity can be considered as a proxy of ionospheric F-region Pedersen conductivity, because the 630-nm airglow is caused by collision between F-region O^+ ions and the neutral O_2 in the thermosphere (e.g., Makela & Kelley, 2003; Sobral et al., 1993). If the polarization electric field associated with MSTIDs is mapped to the magnetosphere and observed by Arase, we should have correlation between the electric field variations observed by Arase and airglow intensity variations at the satellite footprint locations in the ionosphere. As shown by Figure 11 of Kawai et al. (2021), the polarization electric field can also cause electron density variations in the magnetosphere due to $\mathbf{E} \times \mathbf{B}$ drift of magnetospheric plasma which usually has an inward radial gradient (e.g., Carpenter & Anderson, 1992). Thus, we also expect correlation between the electron density variations observed by Arase and the airglow intensity variations at the footprint locations. The correlation can be either positive or negative, depending on the direction of polarization electric field and the direction of density gradient. Thus, we investigated absolute values of correlation coefficient between airglow intensity variations ΔI at satellite footprint locations and electric field variations (ΔE_x, ΔE_y) and electron density variations ΔNe observed by Arase.

Table 2 summarizes a list of conjugate observation events of nighttime MSTIDs obtained by the ground airglow imagers and the Arase satellite. The columns represent, from left to right, event number, observation date, station, observation time in magnetic local time (MLT), representative wavelengths and periods, absolute value of corre-

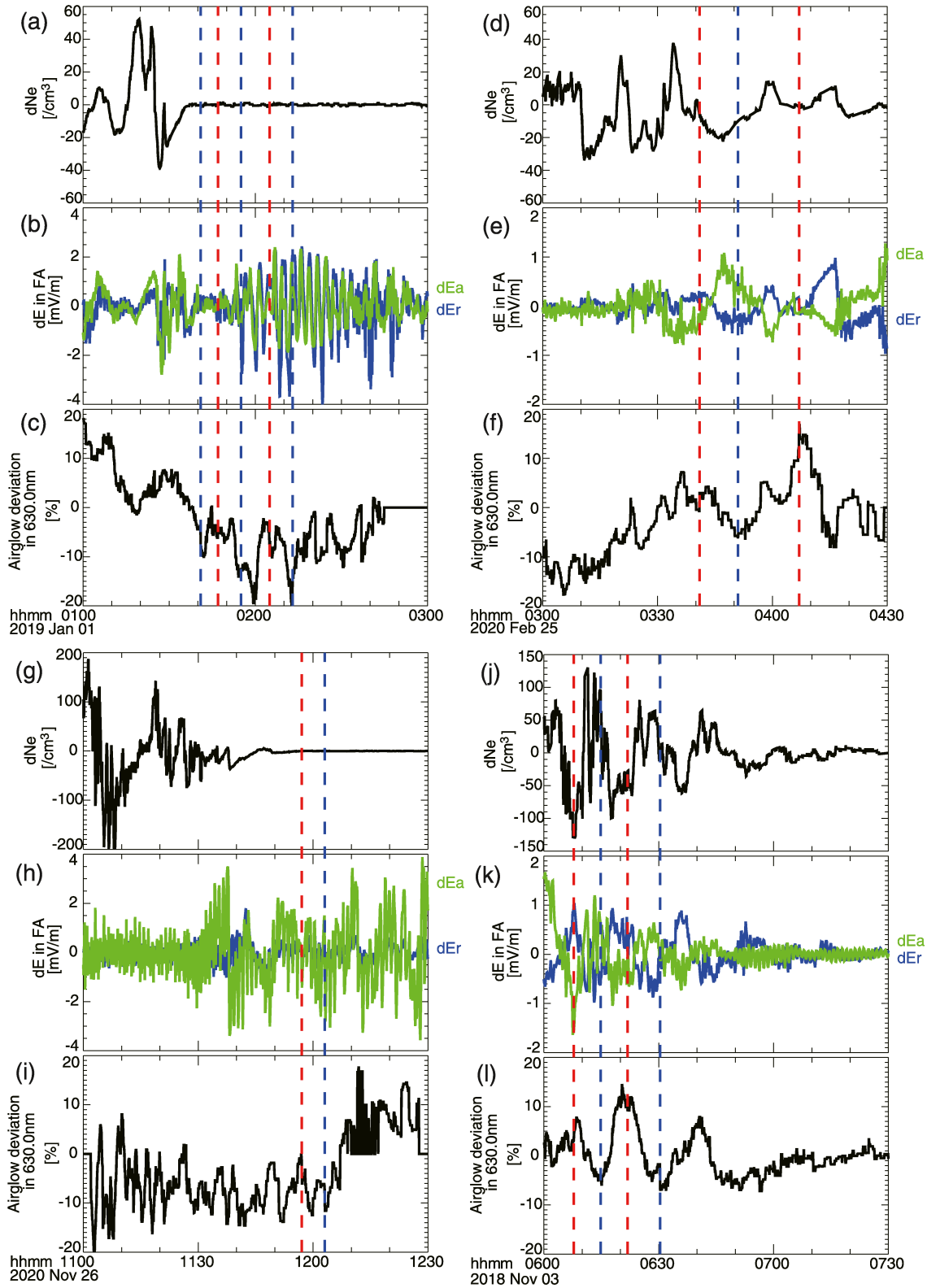

Figure 7. (top) the electron density fluctuations, (middle) the electric field variations in the field-aligned (FA) coordinate, and (bottom) the airglow deviations at the footprint of Arase for the events (a–c) at Athabasca on 1 January 2019, (d–f) at Athabasca on 25 February 2020 (Case 1 in Section 3), (g–i) at Athabasca on 26 November 2020, (j–l) at Gakona on 3 November 2018. The vertical red and blue dashed lines show the times when the Arase satellite footprint crossed the bright and dark parts of the MSTIDs, respectively.

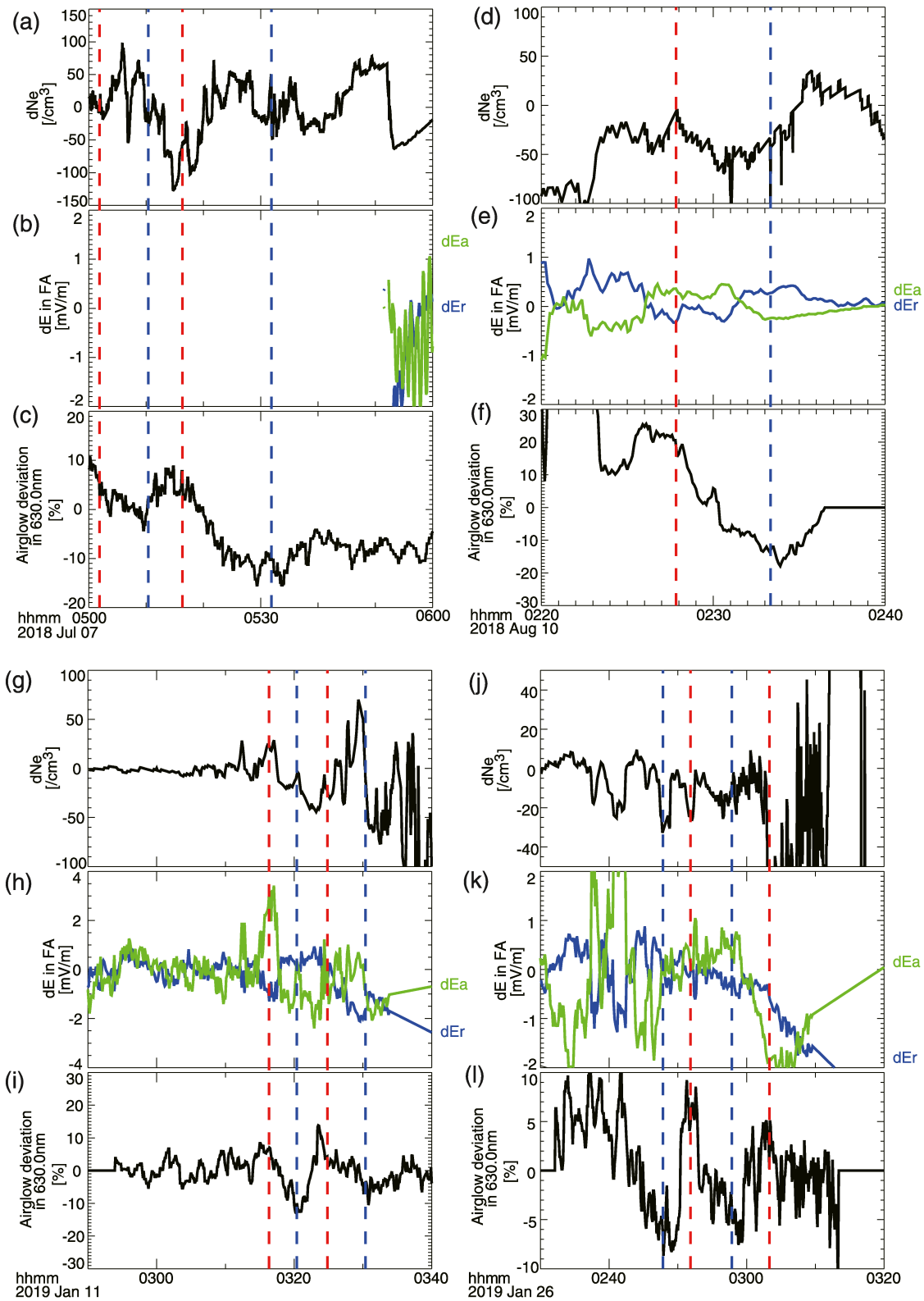

Figure 8. (top) The electron density fluctuations, (middle) the electric field variations in the FA coordinate, and the airglow deviations at the footprint of Arase. This figure shows events all at Kapuskasing (a–c) on 7 July 2018, (d–f) on 10 August 2018, (g–i) on 11 January 2019, (j–l) on 26 January 2019. The vertical red and blue dashed lines of each panel show when the Arase satellite footprint crossed the bright and dark parts of the MSTIDs, respectively.

Table 2
Event List of Simultaneous Observations of Nighttime MSTIDs

Event no.	Date [yyyy/mm/dd]	Station	MLT	Typical wavelength (km)	Typical period (min)	Abs. corr. ΔE_a & ΔI	Abs. corr. ΔE_r & ΔI	Abs. corr. ΔN_e & ΔI	Kp index	MSTID amplitude [%]
No. 1	2019/01/01	ATH	16.9–18.1	100	60	0.071	0.146	0.096	1	20.22
No. 2	2020/02/25	ATH	18.1–19.9	160	40	0.570	0.726	0.426	0^+	18.28
No. 3	2020/11/26	ATH	3.1–5.1	140	60	0.186	0.247	0.558	1	9.48
No. 4	2018/11/03	GAK	19.2–21.2	170	60	0.564	0.616	0.563	0^+	21.77
No. 5	2018/07/07	KAP	0.0–1.5	400	40	No data	No data	0.448	2^-	24.17
No. 6	2018/08/10	KAP	21.5–22.4	160	60	0.519	0.509	0.556	1^+	33.12
No. 7	2019/01/11	KAP	20.2–22.8	250	30	0.173	0.172	0.096	2^-	26.78
No. 8	2019/01/26	KAP	19.8–23.3	180	60	0.186	0.017	0.092	2^-	17.90

lation coefficients between azimuth and radial components of the electric field variations (ΔE_x, ΔE_y) and airglow deviation at the footprint of Arase (ΔI), absolute values of correlation coefficients between electron density fluctuations (ΔNe) and ΔI, the Kp index (Matzka et al., 2021), and the maximum peak-to-peak amplitude of the MSTIDs. The stations are written in abbreviated form: ATH is Athabasca, GAK is Gakona, and KAP is Kapuskasing. The Kp index was used to indicate the disturbance level of background plasma convection and density variation in the magnetosphere. The absolute values of correlation coefficient are calculated for the time interval when the footprint of Arase passes through the phase fronts of the MSTIDs (time interval from leftmost to rightmost dashed lines in Figures 7 and 8). All the events have more than 30 data points for the correlation analysis. The amplitude of the MTSIDs is also calculated by the maximum peak-to-peak amplitudes when the footprint of Arase passes through the phase fronts of the MSTIDs. In this table, we can see that the correlation coefficient between (ΔE_a, ΔE_r) and ΔI, and between ΔNe and ΔI varies in the a range from 0.017 to 0.726.

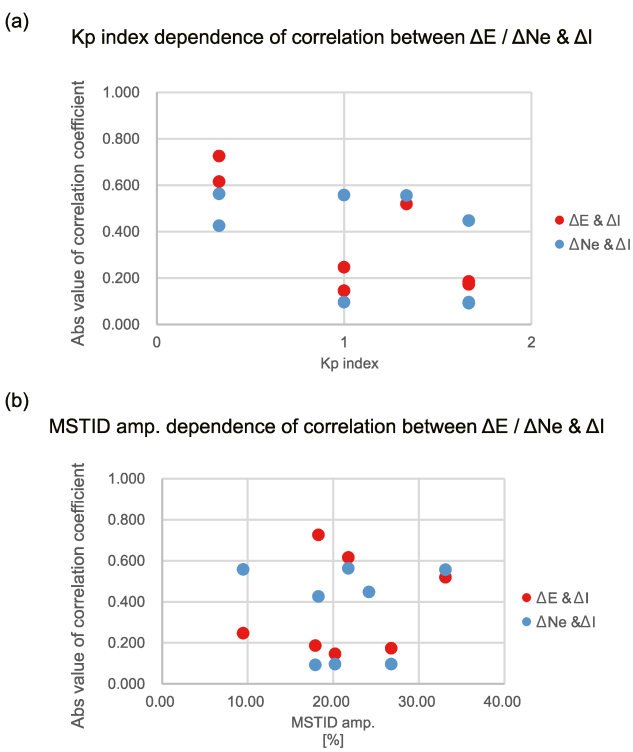

Figure 9. (a) Dependence of absolute values of correlation coefficients between ΔE and ΔI (red dots) and between ΔNe and ΔI (blue dots) on the Kp index, (b) dependence of the correlation coefficients on the amplitude of the MSTIDs. For the absolute values of the correlation coefficients between ΔE and ΔI, only the larger correlation values between ΔE_a and ΔI and between ΔE_r and ΔI are used.

Figure 9a is a scatter plot of these absolute values of the correlation coefficients between ΔE and ΔI (red dots) and between ΔNe and ΔI (blue dots) as a function of the Kp index. Figure 9b is a similar plot of the correlation coefficients as a function of MSTID amplitudes. For the correlation coefficients of electric fields, larger correlation values between ΔE_a and ΔI and between ΔE_r and ΔI are used, because it is difficult to identify direction of MSTID phase surface relative to the azimuth and radial components in FA coordinates at the Arase location.

In Figure 9a, when the Kp index is small, the absolute values of the correlation coefficients tend to be high for both between ΔE and ΔI (correlation coefficient: −0.754) and between ΔNe and ΔI (correlation coefficient: −0.465), though the numbers of data points are only 7–8. In other words, when the Kp index is small, the electric field and density structures of MSTIDs tend to be observed in the magnetosphere. There are a few events where the correlation between ΔE and ΔI and between ΔNe and ΔI is high even if the Kp index is large (e.g., event No. 6).

The 3-hr Kp index indicates the disturbance level of background plasma convection and density variation in the magnetosphere. The Kp index has been also used to parameterize magnetospheric electric field geometry and strength in the equatorial plane (e.g., McIlwain, 1986; Thomsen, 2004). With increasing the Kp value, plasma and electromagnetic disturbances originating from the magnetosphere would occur, such as those associated with plasma injection during substorms. These disturbances originating from the magnetosphere occur independently from the MSTIDs in the ionosphere, and

Table 3
Event List When MSTIDs Are Classified as I-Type and G-Type

Event no.	Date [yyyy/mm/dd]	Station	MLT	Abs. corr. ΔE & ΔI	Abs. corr. ΔN_e & ΔI	Major propagation direction	Phase front	MSTID type
No. 1	2019/01/01	ATH	16.9–18.1	0.146	0.096	W	N-S	I-type
No. 2	2020/02/25	ATH	18.1–19.9	0.726	0.426	W	N-S	I-type
No. 3	2020/11/26	ATH	3.1–5.1	0.247	0.558	E	N-S	I-type
No. 4	2018/11/03	GAK	19.2–21.2	0.616	0.563	W	NW-SE	I-type
No. 5	2018/07/07	KAP	0.0–1.5	No data	0.448	NE & W	NW-SE	G-type
No. 6	2018/08/10	KAP	21.5–22.4	0.519	0.556	NE & W	NW-SE	G-type
No. 7	2019/01/11	KAP	20.2–22.8	0.173	0.096	W	NW-SE	I-type
No. 8	2019/01/26	KAP	19.8–23.3	0.186	0.092	W	NW-SE	I-type

will cause the decrease of the correlation between the airglow variation in the ionosphere and electric field and density variations in the magnetosphere.

In Figure 9b, when the amplitude of MSTIDs is large, the absolute values of the correlation coefficients between ΔE and ΔI tend to be high (correlation coefficient: 0.191). On the other hand, the absolute values of the correlation coefficients between ΔNe and ΔI tend to be independent of the amplitude of the MSTIDs (correlation coefficient: −0.011), though the numbers of data points are only 7–8. The amplitude of MSTIDs depends not only the polarization electric field amplitude but also the vertical gradient of plasma density in the bottomside F-layer, because the 630-nm airglow is caused by interaction of F-layer O^+ ions with the neutral O_2 atmosphere. This effect may contribute to reducing the correlation between the MSTID amplitudes and magnetospheric signatures.

Next, we discuss the characteristics of the MSTIDs. We can classify the MSTIDs observed in this study into two types: I-type and G-type. The I-type MSTIDs, which seem to be caused by the ionospheric plasma instabilities such as Perkins and E-F coupling instabilities, have the following characteristics in airglow images: (a) showing sudden change of propagation direction possibly associated with auroral and geomagnetic field variations (e.g., Shiokawa et al., 2012; Yadav et al., 2020), and sometimes (b) showing ripple-like secondary-instability structures at the light-dark boundary of the MSTIDs (e.g., Makela et al., 2006; Rohrbaugh et al., 1989; Shiokawa et al., 2012; Tsunoda, 1983). The G-type MSTIDs, which seem to be caused by gravity waves in the thermosphere, have the following characteristics in airglow images: (a) invading continuously into the aurora seen in the northern part of the airglow images, (b) having more sinusoidal phase structures, and (c) propagating uni-directionally, and not showing temporal change of the propagation direction. The former-type (I-type) MSTIDs have been reported by Shiokawa et al. (2012) and Yadav et al. (2020). The latter-type (G-type) MSTIDs have been reported by Shiokawa et al. (2013), particularly at summertime in Athabasca in their analysis.

Table 3 summarizes the MSTIDs observed in this study into two types (I-type and G-type). The columns represent, from left to right, event number, observation date, station, observation time in MLT, absolute value of correlation coefficients between ΔE and ΔI, absolute values of correlation coefficients between ΔNe and ΔI, propagation direction of the MSTIDs, phase front of the MSTIDs, and the type of the MSTIDs. The absolute value of correlation coefficients between ΔE and ΔI shows only larger values in the azimuth or radial components.

Two of the eight events were classified as the G-type MSTIDs and the others were classified as the I-type MSTIDs. The G-type MSTIDs were observed at Kapuskasing in summer, showing propagation in two directions per each event, northeastward (NE) and westward (W). The I-type MSTIDs, except for Event 3, propagate mainly westward with a north-south (N-S) or northwest-southeast (NW-SE) phase front. Only the MSTIDs of Event 3 propagates eastward. The I-type MSTIDs are mostly observed on the dusk side, but only the MSTID of Event 3 is observed on the dawn side. This local time-propagation direction tendency is consistent with the direction of typical plasma convection patterns at subauroral latitudes (e.g., Heppner & Maynard, 1987; Weimer, 2005), suggesting that these I-type MSTID propagation is controlled by the background plasma convection. In that case the propagation direction may not be perpendicular to the phase front of the MSTIDs, as shown in Table 3.

The absolute values of correlation coefficients tend to be independent of these MSTID types. Several events have high correlation for both I-type and G-type of the MSTIDs. The I-type MSTIDs are considered as those caused by the Perkins and E-F coupling ionospheric instabilities (e.g., Perkin, 1973; Yokoyama et al., 2009), and

thus, variations in the electric field and plasma density should be caused by the instability. As for the G-type MSTIDs, when the neutral winds due to gravity waves have a component perpendicular to the geomagnetic field lines, polarization electric field could be generated by the neutral wind through the F region dynamo (e.g., Chou et al., 2018, 2022; Liu & Vadas, 2013). Because gravity waves are an oscillation of the neutral winds, oscillating polarization electric fields could be generated. If the amplitude of gravity waves in neutral wind U is 10 m/s under the background magnetic field intensity B of 50,000 nT, it can cause maximum electric field E of 5 mV/m through the F-region dynamo. The electric fields associated with gravity waves in the thermosphere have been observed by incoherent scatter radars (e.g., Varney et al., 2009; Zhang et al., 2021).

5. Conclusions

Based on multi-point ground-satellite observations of MSTIDs over 4 years, we investigated the magnetosphere-ionosphere coupling during appearance of nighttime MSTIDs using airglow imagers installed at Athabasca, Gakona, and Kapuskasing at subauroral latitudes and the Arase satellite near the equatorial plane of the magnetosphere. We found eight simultaneous observations of MSTIDs. The results are summarized as follows.

1. Electric field variations and electron density fluctuations associated with the MSTIDs are not always observed in the magnetosphere.
2. When the Kp index is small or the MSTID amplitude is large, the absolute values of correlation coefficients tend to be high between Arase electric field variations and MSTIDs. These facts indicate that the electric field associated with MSTIDs tends to be mapped to the magnetosphere during magnetically quiet time and for larger MSTID amplitudes.
3. Arase observed the electric field variations and the electron density fluctuations associated with both I-type MSTIDs (possibly caused by ionospheric instabilities) and G-type MSTIDs (possibly caused by gravity waves).

These results indicate that magnetosphere-ionosphere coupling occurs associated with MSTIDs at subauroral latitudes and the coupling is affected by background conditions in the magnetosphere. The coupling of MSTIDs with the magnetosphere and the conjugate ionosphere in the other hemisphere will affect the growth and decay of MSTIDs (e.g., Narayanan et al., 2018). The coupling will also affect radio wave propagation from the magnetosphere to the ionosphere by providing small-scale density structures in the magnetosphere.

Data Availability Statement

The Kp index was provided by the GeoForschungsZentrum (GFZ) Potsdam, Germany through https://www.gfz-potsdam.de/en/kp-index/. The scientific data of the ERG (Arase) satellite were obtained from the ERG Science Center operated by the Institute of Space and Astronautical Science (ISAS), Japan Aerospace Exploration Agency (JAXA) and ISEE, Nagoya University (https://ergsc.isee.nagoya-u.ac.jp/index.shtml.en; Miyoshi, Hori, et al., 2018). The present study analyzed PWE/HFA (level 2, version 1.02; Kasahara, Kumamoto, et al., 2018), and MGF (level 2, version 3.04; Matsuoka et al., 2018a, 2018b), PWE/EFD (level 2, version 5.01; Kasahara, Kasaba, Matsuda, et al., 2018). The airglow images obtained by all-sky cameras at subauroral stations are available from the ISEE through the ERG Science Center.

Acknowledgments
We thank Yasuo Katoh, Yoshiyuki Hamaguchi, Yuka Yamamoto, and Takumi Adachi, technical staff of the ISEE at Nagoya University, for their helpful support when installing the ground-based airglow imagers at Athabasca, Gakona, and Kapuskasing. The airglow imagers installed are optically calibrated at the National Institute of Polar Research (Ogawa et al., 2020). Database construction for the PWING ground-based instruments was supported by the ERG Science Center (https://ergsc.isee.nagoya-u.ac.jp/) and the Inter-university Upper atmosphere Global Observation Network (IUGONET) project (http://www.iugonet.org/). Data from the PWING ground-based instruments are available on these websites. Science data of the ERG (Arase) satellite were obtained from the ERG Science Center operated by ISAS/JAXA and ISEE/Nagoya University (http://ergsc.isee.nagoya-u.ac.jp/, see Miyoshi, Hori, et al., 2018). The Arase satellite datasets for this research are available in these in-text data citation references: Kasahara, Kumamoto, et al. (2018), Kasahara, Kasaba, Matsuda, (2018), Matsuoka et al. (2018a, 2018b). The Kp index data resources are available at https://www.gfz-potsdam.de/en/kp-index/. This work was supported by 15H05815 (Y. Miyoshi), 16H06286 (K. Shiokawa and Y. Miyoshi), 20H01959 (Y. Miyoshi), 15H05747 (S. Oyama and Y. Miyoshi), 21H04518 (K. Shiokawa), JPJSBP120214805 (K. Shiokawa), and JPJSCCB20210003 (K. Shiokawa) of Japan Society for the Promotion of Science. The observatory housing the Athabasca instrument was constructed and is operated with funding from the Canada Foundation for Innovation and we thank Ian Schofield for assistance.

References

Alken, P., Thébault, E., Beggan, C. D., Amit, H., Aubert, J., Baerenzung, J., et al. (2021). International geomagnetic reference field: The thirteenth generation. *Earth Planets and Space*, *73*(1), 49. https://doi.org/10.1186/s40623-020-01288-x

Angelopoulos, V., Cruce, P., Drozdov, A., Grimes, E. W., Hatzigeorgiu, N., King, D. A., et al. (2019). The space physics environment data analysis system (SPEDAS). *Space Science Reviews*, *215*(1), 9. https://doi.org/10.1007/s11214-018-0576-4

Bowman, G. G. (1990). A review of some recent work on mid-latitude Spread-F occurrence as detected by ionosondes. *Journal of Geomagnetism and Geoelectricity*, *42*(2), 109–138. https://doi.org/10.5636/jgg.42.109

Carpenter, D. L., & Anderson, R. R. (1992). An ISEE/Whistler model of equatorial electron density in the magnetosphere. *Journal of Geophysical Research*, *97*(A2), 1097–1108. https://doi.org/10.1029/91JA01548

Chen, Y., Friedel, R. H. W., & Reeves, G. D. (2006). Phase space density distributions of energetic electrons in the outer radiation belt during two Geospace Environment Modeling Inner Magnetosphere/Storms selected storms. *Journal of Geophysical Research*, *111*(A11S04), A11S04. https://doi.org/10.1029/2006JA011703

Chou, M.-Y., Lin, C. C. H., Huba, J. D., Lien, C.-P., Chen, C.-H., Yue, J., et al. (2018). Numerical modeling of the concentric gravity wave seeding of low-latitude nighttime medium-scale traveling ionospheric disturbances. *Geophysical Research Letters*, *45*(13), 6390–6399. https://doi.org/10.1029/2018GL077959

Chou, M.-Y., Yue, J., Lin, C. C. H., Rajesh, P. K., & Pedatella, N. M. (2022). Conjugate effect of the 2011 Tohoku reflected tsunami-driven gravity waves in the ionosphere. *Geophysical Research Letters*, *49*(3), e2021GL097170. https://doi.org/10.1029/2021GL097170

Cosgrove, R. B., & Tsunoda, R. T. (2001). Polarization electric fields sustained by closed-current dynamo structures in midlatitude sporadic E. *Geophysical Research Letters*, *28*(8), 1455–1458. https://doi.org/10.1029/2000GL012178

Cosgrove, R. B., & Tsunoda, R. T. (2004). Instability of the E–F coupled nighttime midlatitude ionosphere. *Journal of Geophysical Research*, *109*(A4), A04305. https://doi.org/10.1029/2003JA010243

Fukushima, D., Shiokawa, K., Otsuka, Y., & Ogawa, T. (2012). Observation of equatorial nighttime medium-scale traveling ionospheric disturbances in 630-nm airglow images over 7 years. *Journal of Geophysical Research*, *117*(A10), A10324. https://doi.org/10.1029/2012JA017758

Heppner, J. P., & Maynard, N. C. (1987). Empirical high-latitude electric field models. *Journal of Geophysical Research*, *92*(A5), 4467–4489. https://doi.org/10.1029/JA092iA05p04467

Hunsucker, R. D. (1982). Atmospheric gravity waves generated in the high-latitude ionosphere: A review. *Review of Geophysics*, *20*(2), 293–315. https://doi.org/10.1029/RG020i002p00293

Kasaba, Y., Ishisaka, K., Kasahara, Y., Imachi, T., Yagitani, S., Kojima, H., et al. (2017). Wire probe antenna (WPT) and electric field detector (EFD) of plasma wave experiment (PWE) aboard the Arase satellite: Specifications and initial evaluation results. *Earth Planets and Space*, *69*(1), 174. https://doi.org/10.1186/s40623-017-0760-x

Kasahara, Y., Kasaba, Y., Kojima, H., Yagitani, S., Ishisaka, K., Kumamoto, A., et al. (2018). The plasma wave experiment (PWE) on board the Arase (ERG) satellite. *Earth Planets and Space*, *70*(1), 86. https://doi.org/10.1186/s40623-018-0842-4

Kasahara, Y., Kasaba, Y., Matsuda, S., Shoji, M., Nakagawa, T., Ishisaka, K., et al. (2018). *The PWE/EFD instrument Level-2 spin-fit electric field data of Exploration of energization and Radiation in Geospace (ERG) Arase satellite, Version v05.01*. ERG Science Center, Institute for Space-Earth Environmental Research, Nagoya University. Accessed 2022-03-23. https://doi.org/10.34515/DATA.ERG-07000

Kasahara, Y., Kumamoto, A., Tsuchiya, F., Matsuda, S., Shoji, M., Nakamura, S., et al. (2018). *The PWE/HFA instrument Level-2 spectrum data of Exploration of energization and Radiation in Geospace (ERG) Arase satellite, Version v01.02*. ERG Science Center, Institute for Space-Earth Environmental Research, Nagoya University. Updated daily. Accessed 2022-03-23. https://doi.org/10.34515/DATA.ERG-10000

Kawai, K., Shiokawa, K., Otsuka, Y., Oyama, S., Kasaba, Y., Kasahara, Y., et al. (2021). First simultaneous observation of a nighttime medium-scale traveling ionospheric disturbance from the ground and a magnetospheric satellite. *Journal of Geophysical Research*, *126*(9). https://doi.org/10.1029/2020JA029086

Kubota, M., Conde, M., Ishii, M., Murayama, Y., & Jin, H. (2011). Characteristics of nighttime medium-scale traveling ionospheric disturbances observed over Alaska. *Journal of Geophysical Research*, *116*(A5), A05307. https://doi.org/10.1029/2010JA016212

Kumamoto, A., Tsuchiya, F., Kasahara, Y., Kasaba, Y., Kojima, H., Yagitani, S., et al. (2018). High frequency analyzer (HFA) of plasma wave experiment (PWE) onboard the Arase spacecraft. *Earth Planets and Space*, *70*(1), 82. https://doi.org/10.1186/s40623-018-0854-0

Liu, H.-L., & Vadas, S. L. (2013). Large-scale ionospheric disturbances due to the dissipation of convectively generated gravity waves over Brazil. *Journal of Geophysical Research: Space Physics*, *118*(5), 2419–2427. https://doi.org/10.1002/jgra.50244

Makela, J. J., & Kelley, M. C. (2003). Using the 630.0-nm nightglow emission as a surrogate for the ionospheric Pedersen conductivity. *Journal of Geophysical Research*, *108*(A6), 1253. https://doi.org/10.1029/2003ja009894

Makela, J. J., Kelley, M. C., & Nicolls, M. J. (2006). Optical observations of the development of secondary instabilities on the eastern wall of an equatorial plasma bubble. *Journal of Geophysical Research*, *111*(A9), A09311. https://doi.org/10.1029/2006JA011646

Martinis, C., Baumgardner, J., Mendillo, M., Wroten, J., MacDonald, T., Kosch, M., et al. (2018). First conjugate observations of medium-scale traveling ionospheric disturbances (MSTIDs) in the Europe-Africa longitude sector. *Journal of Geophysical Research*, *124*(3), 2213–2222. https://doi.org/10.1029/2018JA026018

Martinis, C., Baumgardner, J., Wroten, J., & Mendillo, M. (2011). All-sky imaging observations of conjugate medium-scale traveling ionospheric disturbances in the American sector. *Journal of Geophysical Research*, *116*(A5), A05326. https://doi.org/10.1029/2010JA016264

Matsuoka, A., Teramoto, M., Imajo, S., Kurita, S., Miyoshi, Y., & Shinohara, I. (2018a). *The MGF instrument level-2 high-resolution magnetic field data of Exploration of energization and Radiation in Geospace (ERG) Arase satellite, Version v03.04*. ERG Science Center, Institute for Space-Earth Environmental Research, Nagoya University. Updated daily. Accessed 2022-03-23. https://doi.org/10.34515/DATA.ERG-06000

Matsuoka, A., Teramoto, M., Imajo, S., Kurita, S., Miyoshi, Y., & Shinohara, I. (2018b). *The MGF instrument level-2 spin-averaged magnetic field data of Exploration of energization and Radiation in Geospace (ERG) Arase satellite, Version v03.04*. ERG Science Center, Institute for Space-Earth Environmental Research, Nagoya University. Updated daily. Accessed 2022-03-23. https://doi.org/10.34515/DATA.ERG-06001

Matsuoka, A., Teramoto, M., Nomura, R., Nose, M., Fujimoto, A., Tanaka, Y., et al. (2018). The ARASE (ERG) magnetic field investigation. *Earth Planets and Space*, *70*(1), 43. https://doi.org/10.1186/s40623-018-0800-1

Matzka, J., Stolle, C., Yamazaki, Y., Bronkalla, O., & Morschhauser, A. (2021). The geomagnetic Kp index and derived indices of geomagnetic activity. *Space Weather*, *19*(5). https://doi.org/10.1029/2020SW002641

McIlwain, C. E. (1986). A Kp dependent equatorial electric field model. *Advances in Space Research*, *6*(3), 187–197. https://doi.org/10.1016/0273-1177(86)90331-5

Mendillo, M., Baumgardner, J., Nottingham, D., Aarons, J., Reinisch, B., Scali, J., & Kelley, M. (1997). Investigations of thermospheric-ionospheric dynamics with 6300-Å images from Arecibo observatory. *Journal of Geophysical Research*, *102*(A4), 7331–7343. https://doi.org/10.1029/96JA02786

Miyoshi, Y., Hori, T., Shoji, M., Teramoto, M., Chang, T. F., Matsuda, S., et al. (2018). The ERG science center. *Earth Planets and Space*, *70*(1), 96. https://doi.org/10.1186/s40623-018-0867-8

Miyoshi, Y., Shinohara, I., Takashima, T., Asamura, K., Higashio, N., Mitani, T., et al. (2018). Geospace exploration project ERG. *Earth Planets and Space*, *70*(1), 101. https://doi.org/10.1186/s40623-018-0862-0

Moral, A. C., Shiokawa, K., Suzuki, S., Liu, H., Otsuka, Y., & Yatini, C. Y. (2019). Observations of low-latitude traveling ionospheric disturbances by a 630.0-nm airglow imager and the CHAMP satellite over Indonesia. *Journal of Geophysical Research: Space Physics*, *124*(3), 2198–2212. https://doi.org/10.1029/2018JA025634

Narayanan, V. L., Shiokawa, K., Otsuka, Y., & Neudegg, D. (2018). On the role of thermospheric winds and sporadic E layers in the formation and evolution of electrified MSTIDs in geomagnetic conjugate regions. *Journal of Geophysical Research: Space Physics*, *123*(8), 6957–6980. https://doi.org/10.1029/2018JA025261

Ogawa, Y., Kadokura, A., & Ejiri, M. K. (2020). Optical calibration system of NIPR for aurora and airglow observations. *Polar Science*, 100570. https://doi.org/10.1016/j.polar.2020.100570

Otsuka, Y., Shiokawa, K., Ogawa, T., & Wilkinson, P. (2004). Geomagnetic conjugate observations of medium-scale traveling ionospheric disturbances at midlatitude using all sky imagers. *Geophysical Research Letters*, *31*(15), L15803. https://doi.org/10.1029/2004GL020262

Otsuka, Y., Suzuki, K., Nakagawa, S., Nishioka, M., Shiokawa, K., & Tsugawa, T. (2013). GPS observations of medium-scale traveling ionospheric disturbances over Europe. *Annales Geophysicae*, *31*(2), 163–172. https://doi.org/10.5194/angeo-31-163-2013

Perkin, F. (1973). Spread F and ionospheric currents. *Journal of Geophysical Research*, *78*(1), 218–226. https://doi.org/10.1029/JA078i001p00218

Rohrbaugh, R. P., Hanson, W. B., Tinsley, B. A., Cragin, B. L., McClure, J. P., & Broadfoot, A. L. (1989). Images of transequatorial bubbles based on field-aligned airglow observations from Haleakala in 1984-1986. *Journal of Geophysical Research*, *94*(A6), 6763–6770. https://doi.org/10.1029/JA094iA06p06763

Saito, A., Iyemori, T., Blomberg, L. G., Yamamoto, M., & Takeda, M. (1998). Conjugate observations of the mid-latitude electric field fluctuations with the MU radar and the Freja satellite. *Journal of Atmospheric and Solar-Terrestrial Physics*, *60*(1), 129–140. https://doi.org/10.1016/S1364-6826(97)00094-1

Shiokawa, K., Katoh, Y., Hamaguchi, Y., Yamamoto, Y., Adachi, T., Ozaki, M., et al. (2017). Ground-based instruments of the PWING project to investigate dynamics of the inner magnetosphere at subauroral latitudes as a part of the ERG-ground coordinated observation network. *Earth Planets and Space*, *69*(1), 160. https://doi.org/10.1186/s40623-017-0745-9

Shiokawa, K., Katoh, Y., Satoh, M., Ejiri, M. K., Ogawa, T., Nakamura, T., et al. (1999). Development of optical mesosphere thermosphere imagers (OMTI). *Earth Planets and Space*, *51*(7–8), 887–896. https://doi.org/10.1186/BF03353247

Shiokawa, K., Mori, M., Otsuka, Y., Oyama, S., & Nozawa, S. (2012). Motion of high-latitude nighttime medium-scale traveling ionospheric disturbances associated with auroral brightening. *Journal of Geophysical Research*, *117*(A10), A10316. https://doi.org/10.1029/2012JA017928

Shiokawa, K., Mori, M., Otsuka, Y., Oyama, S., Nozawa, S., Suzuki, S., & Connors, M. (2013). Observation of nighttime medium-scale traveling ionospheric disturbances by two 630-nm airglow imagers near the auroral zone. *Journal of Atmospheric and Solar-Terrestrial Physics*, *103*, 184–194. https://doi.org/10.1016/j.jastp.2013.03.024

Shiokawa, K., Otsuka, Y., Ihara, C., Ogawa, T., & Rich, F. J. (2003). Ground and satellite observations of night time medium-scale traveling ionospheric disturbance at midlatitude. *Journal of Geophysical Research*, *108*(A4), 1145. https://doi.org/10.1029/2002JA009639

Shiokawa, K., Otsuka, Y., Tsugawa, T., Ogawa, T., Saito, A., Ohshima, K., et al. (2005). Geomagnetic conjugate observation of night time medium-scale and large-scale traveling ionospheric disturbances: FRONT3 campaign. *Journal of Geophysical Research*, *110*(A5), A05303. https://doi.org/10.1029/2004JA010845

Sobral, J. H. A., Takahashi, H., Abdu, M. A., Muralikrishna, P., Sahai, Y., Zamlutti, C. J., et al. (1993). Determination of the quenching rate of the O(1D) by O(3P) from rocket-borne optical (630 nm) and electron density data. *Journal of Geophysical Research*, *98*(A5), 7791–7798. https://doi.org/10.1029/92ja01839

Taylor, M. J., Jahn, J.-M., Fukao, S., & Saito, A. (1998). Possible evidence of gravity wave coupling into the mid-latitude F region ionosphere during the SEEK campaign. *Geophysical Research Letters*, *25*(11), 1801–1804. https://doi.org/10.1029/97GL03448

Thomsen, M. F. (2004). Why Kp is such a good measure of magnetospheric convection. *Space Weather*, *2*(11), S11004. https://doi.org/10.1029/2004sw000089

Tsunoda, R. T. (1983). On the generation and growth of equatorial backscatter plumes: 2. Structuring of the west walls of upwellings. *Journal of Geophysical Research*, *88*(A6), 4869–4874. https://doi.org/10.1029/ja088ia06p04869

Tsyganenko, N. A. (2002a). A model of the near magnetosphere with a dawn-dusk asymmetry 1. Mathematical structure. *Journal of Geophysical Research*, *107*(A8), 1. https://doi.org/10.1029/2001JA000219

Tsyganenko, N. A. (2002b). A model of the near magnetosphere with a dawn-dusk asymmetry 2. Parameterization and fitting to observations. *Journal of Geophysical Research*, *107*(A8), 1. https://doi.org/10.1029/2001JA000220

Tsyganenko, N. A., & Sitnov, M. I. (2005). Modeling the dynamics of the inner magnetosphere during strong geomagnetic storms. *Journal of Geophysical Research*, *110*(A3), A03208. https://doi.org/10.1029/2004JA010798

Varney, R. H., Kelley, M. C., & Kudeki, E. (2009). Observations of electric fields associated with internal gravity waves. *Journal of Geophysical Research*, *114*(A2), A02304. https://doi.org/10.1029/2008JA013733

Weimer, D. R. (2005). Improved ionospheric electrodynamic models and application to calculating Joule heating rates. *Journal of Geophysical Research*, *110*(A5), A05306. https://doi.org/10.1029/2004JA010884

Yadav, S., Shiokawa, K., Oyama, S., & Otsuka, Y. (2020). Multievent analysis of oscillatory motion of medium-scale traveling ionospheric disturbances observed by a 630-nm airglow imager over Tromsø. *Journal of Geophysical Research*, *125*(3), e2019JA027598. https://doi.org/10.1029/2019JA027598

Yokoyama, T., Horinouchi, T., Yamamoto, M., & Fukao, S. (2004). Modulation of the midlatitude ionospheric E region by atmospheric gravity waves through polarization electric field. *Journal of Geophysical Research*, *109*(A12), A12307. https://doi.org/10.1029/2004JA010508

Yokoyama, T., & Hysell, D. L. (2010). A new midlatitude ionosphere electrodynamics coupling model (MIECO): Latitudinal dependence and propagation of medium-scale traveling ionospheric disturbances. *Geophysical Research Letters*, *37*(8), L08105. https://doi.org/10.1029/2010GL042598

Yokoyama, T., Hysell, D. L., Otsuka, Y., & Yamamoto, M. (2009). Three-dimensional simulation of the coupled Perkins and Es-layer instabilities in the nighttime midlatitude ionosphere. *Journal of Geophysical Research*, *114*(A3), A03308. https://doi.org/10.1029/2008JA013789

Zhang, S.-R., Erickson, P. J., Gasque, L. C., Aa, E., Rideout, W., Vierinen, J., et al. (2021). Electrified postsunrise ionospheric perturbations at Millstone Hill. *Geophysical Research Letters*, *48*(18), e2021GL095151. https://doi.org/10.1029/2021GL095151